Axisymmetric lattice Boltzmann model for simulating the freezing process of a sessile water droplet with volume change

Chaoyang Zhang,[1] Hui Zhang,[1] Wenzhen Fang,[1] Yugang Zhao,[2] and Chun Yang[1,*]

[1]*School of Mechanical and Aerospace Engineering, Nanyang Technological University, 50 Nanyang Avenue, Singapore 639798, Singapore*

[2]*School of Energy and Power Engineering, University of Shanghai for Science and Technology, 516 Jun Gong Road, Shanghai, 200093, China*

(Received 7 September 2019; accepted 5 February 2020; published 26 February 2020)

Droplet freezing not only is of fundamental interest but also plays an important role in numerous natural and industrial processes. However, it is challenging to numerically simulate the droplet freezing process due to its involving a complex three-phase system with dynamic phase change and heat transfer. Here we propose an axisymmetric lattice Boltzmann (LB) model to simulate the freezing process of a sessile water droplet with consideration of droplet volume expansion. Combined with the multiphase flow LB model and the enthalpy thermal LB model, our proposed approach is applied to simulate the sessile water droplet freezing on both hydrophilic and hydrophobic surfaces at a fixed subcooled temperature. Through comparison with the experimental counterpart, the comparison results show that our axisymmetric LB model can satisfactorily describe such sessile droplet freezing processes. Moreover, we use both LB simulations and analytical models to study the effects of contact angle and volume expansion on the freezing time and the cone shape formed on the top of frozen droplets. The analytical models are obtained based on heat transfer and geometric analyses. Additionally, we show analytically and numerically that the freezing front-to-interface angle keeps nearly constant (smaller than 90°).

DOI: 10.1103/PhysRevE.101.023314

I. INTRODUCTION

Liquid droplet freezing on cold surfaces is a common phase change phenomenon happening in our daily life and many industrial processes such as refrigeration, aerospace, food processing, pharmaceutical manufacturing, etc. Undesirable water droplet freezing can threaten the safety of society in subzero environments and deteriorate the performance of heat exchange equipment. Therefore, many anti-icing and de-icing studies, focusing on searching for the effective icing resistance methods, have been conducted in recent decades [1].

Single-droplet freezing is often used as a model system to explore the underlying freezing mechanisms [2–5]. For a water droplet freezing on a subcooled surface, the droplet final frozen shape is pointed with a sharp tip. To explain such tip formation, numerous experimental and theoretical studies have been reported [6–15]. The volume expansion change due to ice density shrinking was proposed as a major factor for the tip formation, and the tip shape with a cone angle is considered a universal value that depends on the density ratio of water to ice [10]. Moreover, the surface tension makes the unfrozen liquid have inward contraction of the triple-contact line. For quantitative analyses, Anderson *et al.* discussed four analytical conditions at the trijunction: the fixed contact angle, fixed contact line, fixed growth angle, and dynamic growth angle; and through comparison with the experiments they found that only the dynamic growth angle is seen satisfactorily [6]. Moreover, two freezing front shapes are assumed: one is flat [6], and the other is curved with its edge perpendicular to the droplet interface [10]. When heat transfer is considered, Vu *et al.* [12,13] applied the front-tracking method to numerically simulate the water droplet freezing considering the volume change and the ice-water interface propagation. However, their simulation results showed that the freezing process cannot be completely computed because there is always a small amount of liquid inevitably remaining on the droplet tip. Considering the subcooling effect, Zhang *et al.* [14,15] developed a numerical model to handle nucleation and freezing into two stages, and they determined the movement of the freezing front by using a one-dimensional (1D) energy equation and Anderson *et al.*'s [6] contact line slip model. It should be mentioned that the addition of other substances in water may cause a change in the frozen droplet shape. Zhao *et al.* [16] found that when nanoparticles are added into water, the frozen droplet shape exhibits a flat plateau instead of the pointy tip. Singha *et al.* [17] observed that the presence of salinity in water can not only delay the droplet freezing time, but also depress the formation of a pointy top. For these newly reported phenomena, there is still no satisfactory explanation.

The lattice Boltzmann method (LBM) is a numerical approach used for studying complex fluid flow and heat transfer problems, especially for phase-change-associated fluid systems. One-component and multicomponent multiphase models were used to simulate the liquid-vapor phase change processes, including boiling [18], condensation [19], and droplet and film evaporation [20]. In these works, the LBM enables nontracking of the interface and the coupled equation of state (EOS) to adjust the separation of vapor and liquid phases according to the local state parameters. Several

*mcyang@ntu.edu.sg

enthalpy-based LB models were also developed to deal with the solidification (or freezing) and melting processes [21–23]. To our best knowledge, no study has been reported using LBM for simulating the water freezing phenomenon with volume expansion or density change. Our search from the open literature shows that the reported studies are on the use of LBM to simulate water droplet freezing [24–26], in which a two-dimensional (2D) droplet is considered with fixed droplet interface and the same ice and water densities. Li *et al.* [27] conducted a three-dimensional (3D) simulation of the continuous phase change from water vapor condensation to freezing on a cryogenic spot; in their work, the droplet is not completely solidified, and the volume change is not taken into account. Using a multicomponent multiphase LB model, Xiong and Cheng [28] simulated the gas entrainment effect on metal solidification processes. Recently, Gong *et al.* [26,29] presented a 2D mesoscopic model with density change for simulating water droplet freezing [26] and compared the simulation results with their experimental ones.

In this work, we propose an axisymmetric LB model to simulate the entire droplet freezing process with volume change; the model is based on the pseudopotential multiphase LB method for the density field and the enthalpy thermal LB method for the temperature field. Compared to the conventional CFD simulation methods [12–15] and the freezing front models such as Anderson's [6] and Marin's [10], our proposed LB model has two advantages: (1) the motion of the freezing front and triple-phase point can be naturally determined by the enthalpy equation and (2) the water-ice volume expansion effect is introduced as an additional source term in the mass transfer equation at the freezing front. Hence, the growth angle and contact line slipping motion conditions discussed in Ref. [6] are based on force balancing at the tri-junction rather than the use of fitting relationships. We conduct the model validation by comparing with our experiments for a water droplet on a subcooled surface with different contact angle. In our simulations, the droplet shape change during freezing and the final tip formation under various solid-liquid density ratios are studied. Additionally, the cone angle at the tip and the freezing front to interface angle are examined and compared with the assumptions made in previous research work.

II. LATTICE BOLTZMANN MODELS

In this section, the well-known Shan-Chen (SC) multiphase LBM [30] is first outlined in a 2D Cartesian coordinate system. Then the coordinate transformation is presented to obtain an axisymmetric multiphase LBM in a cylindrical coordinate system. The axisymmetric multiphase model is used to construct the droplet-air system. After that, the solid-liquid phase change model with volume change is introduced for the density variation between water and ice phases. Finally, the enthalpy-based thermal LBM in an axisymmetric multiphase system is reported.

A. Shan-Chen (SC) lattice Boltzmann method

To track the liquid-vapor interface, the SC multiphase LB model is adopted. The BGK evolution equation in D2Q9 form is expressed as

$$f_i(\mathbf{x}+\mathbf{e}_i\delta_t, t+\delta_t) - f_i(\mathbf{x},t) = -\frac{1}{\tau}\left[f_i(\mathbf{x},t) - f_i^{\mathrm{eq}}(\mathbf{x},t)\right] + \Delta f_i(\mathbf{x},t) + \delta_t \Phi_i, \quad (1)$$

where f_i is the density distribution function, $\mathbf{x}$ and t, respectively, are the current position and time, $\mathbf{e}_i$ represents the nine velocities set as $[(0,0), (0,\pm1), (\pm1,0), (\pm1,\pm1)]$ c (with c being the lattice velocity), τ is the relaxation time related to the kinematic viscosity ν with $\tau = 3\nu + 0.5$, Φ_i is the mass source term, which will be discussed later, and $f_i^{\mathrm{eq}}(\mathbf{x},t)$ is the corresponding equilibrium distribution function given by

$$f_i^{\mathrm{eq}} = \omega_i \rho\left[1 + \frac{\mathbf{e}_i\cdot\mathbf{u}}{c_s^2} + \frac{(\mathbf{e}_i\cdot\mathbf{u})^2}{2c_s^4} - \frac{\mathbf{u}^2}{2c_s^2}\right], \quad (2)$$

with ω_i being the weighting coefficients and $c_s = 1/\sqrt{3}c$ being the lattice sound speed. $\Delta f_i(\mathbf{x},t)$ in Eq. (1) is the body force term that is specified in the exact difference method [31]

$$\Delta f_i(\mathbf{x},t) = f_i^{\mathrm{eq}}\left[\rho(\mathbf{x},t), \mathbf{u} + \frac{\mathbf{F}\delta_t}{\rho}\right] - f_i^{\mathrm{eq}}(\rho(\mathbf{x},t), \mathbf{u}) \quad (3)$$

in which $\mathbf{F}$ is the total body force term exerting on the particles and is given by

$$\mathbf{F} = \mathbf{F}_f(\mathbf{x}) + \mathbf{F}_s(\mathbf{x}) + \mathbf{F}_g(\mathbf{x}), \quad (4)$$

where $\mathbf{F}_f$ is the interparticle interaction force, $\mathbf{F}_s$ is the fluid-solid interaction force, and $\mathbf{F}_g$ is the gravitational force. Based on the method described in Refs. [32–34], $\mathbf{F}_f$ can be calculated as

$$\mathbf{F}_f(\mathbf{x}) = -\beta c_0 \psi(\mathbf{x}) g \nabla\psi(\mathbf{x}) - \frac{(1-\beta)}{2} c_0 g \nabla\psi^2(\mathbf{x}) - \frac{1}{2}c_s^2 c_0 g \psi(\mathbf{x}) \nabla[\nabla^2\psi(\mathbf{x})], \quad (5)$$

where β is the weighting factor, $c_0 = 6$ in D2Q9 and $\psi(\mathbf{x})$ is the so-called "effective mass" given by

$$\psi(\rho(\mathbf{x})) = \sqrt{\frac{2\left(p - \rho c_s^2\right)}{c_0 g}}, \quad (6)$$

where p is calculated from a given EOS, and g is the interaction strength, which will be eliminated in Eq. (5).

From the flow distribution function, the density and velocity in the flow field can be obtained from

$$\rho = \sum_i f_i, \quad (7)$$

$$\rho\mathbf{u} = \sum_i \mathbf{e}_i f_i, \quad (8)$$

and the macrovelocity is updated according to the momentum balance before and after the collision

$$\tilde{\mathbf{u}} = \mathbf{u} + \frac{\mathbf{F}\delta_t}{2\rho}. \quad (9)$$

B. Axisymmetric multiphase lattice Boltzmann model

Here we consider a 2D axisymmetric system in terms of cylindrical coordinates as $\mathbf{x} = (r, z)$ instead of 2D Cartesian

coordinates as $\mathbf{x} = (x, y)$. Hence, the velocity is transformed from $\mathbf{u} = (u_x, u_y)$ into $\mathbf{u} = (u_r, u_z)$. Through comparing the Naiver-Stokes equations expressed in these two coordinate systems, we find that an appropriate source term is needed to recover the axisymmetric continuity equation and the momentum equations [32,33], and these equations are expressed as

$$\frac{\partial \rho}{\partial t} + \nabla_c \cdot (\rho \mathbf{u}) = -\frac{1}{r}\rho u_r, \tag{10}$$

$$\frac{\partial u_r}{\partial t} + u_r\frac{\partial u_r}{\partial r} + u_z\frac{\partial u_r}{\partial z} = -\frac{1}{\rho}\frac{\partial p}{\partial r} + \frac{\mu}{\rho}\left(\nabla_c^2 u_z - \frac{u_r}{r^2}\right), \tag{11}$$

$$\frac{\partial u_z}{\partial t} + u_r\frac{\partial u_z}{\partial r} + u_z\frac{\partial u_z}{\partial z} = -\frac{1}{\rho}\frac{\partial p}{\partial z} + \frac{\mu}{\rho}\nabla_c^2 u_z. \tag{12}$$

Following Srivastava *et al.*'s work [32], we rewrite the evolution of density distribution equation as

$$\begin{aligned} &f_i(\mathbf{x} + \mathbf{e}_i\delta_t, t + \delta_t) - f_i(\mathbf{x}, t) \\ &= -\frac{1}{\tau}\left[f_i(\mathbf{x}, t) - f_i^{\mathrm{eq}}(\mathbf{x}, t)\right] + \Delta f_i(\mathbf{x}, t) \\ &\quad + \delta_t k_i\left(\mathbf{x} + \frac{1}{2}\mathbf{e}_i\delta_t, t + \frac{1}{2}\delta_t\right), \end{aligned} \tag{13}$$

where k_i is the induced source term due to the coordinate transformation, and it has the following form according to Eqs. (10)–(12):

$$k_i = \omega_i\left[-\frac{\rho u_r}{r} + \frac{1}{c_s^2}(e_{iz}K_z + e_{ir}K_r)\right] \tag{14}$$

with

$$K_r = \frac{e_{ir}}{r}\left[2\mu\left(\frac{\partial u_r}{\partial r} - \frac{u_r}{r}\right) - \rho u_r^2\right], \tag{15}$$

$$K_z = \frac{e_{iz}}{r}\left[\mu\left(\frac{\partial u_z}{\partial r} + \frac{\partial u_r}{\partial z}\right) - \rho u_r u_z\right]. \tag{16}$$

Apart from the source term in the evolution equation, the gradient and Laplace operator in the force calculation also should be changed in the cylindrical coordinates according to

$$\nabla\psi = \nabla_c\psi. \tag{17}$$

$$\nabla^2\psi = \nabla_c^2\psi + \frac{1}{r}\frac{\partial\psi}{\partial r}. \tag{18}$$

Therefore, the interaction force between fluid particles should be changed into

$$\begin{aligned} \mathbf{F}_f(\mathbf{x}) &= -\beta c_0\psi(\mathbf{x})g\,\nabla_c\psi(\mathbf{x}) - \frac{(1-\beta)}{2}c_0 g\,\nabla_c\psi^2(\mathbf{x}) \\ &\quad + \frac{1}{2}c_s^2 c_0 g\psi(\mathbf{x})\nabla_c\left[\frac{1}{r}\frac{\partial\psi(\mathbf{x})}{\partial r}\right]. \end{aligned} \tag{19}$$

When dealing with the gradient and Laplace terms, we use the following second-order compact schemes:

$$\frac{\partial\psi}{\partial x} = \frac{1}{2c_s^2\delta_t}\sum_\alpha \omega_i e_i[\psi(\mathbf{x} + e_i) - \psi(\mathbf{x} - e_i)], \tag{20}$$

$$\frac{\partial^2\psi}{\partial x^2} = \frac{1}{c_s^2\delta_t}\sum_\alpha \omega_i e_i[\psi(\mathbf{x} + e_i) + \psi(\mathbf{x} - e_i) - \psi(\mathbf{x})]. \tag{21}$$

C. Solid-liquid phase change with volume change

When freezing occurs, the streaming process of distribution is divided into two parts: the freezing part is bounced back with a fraction B, and the remaining part remains streaming [27]. Then the evolution equation becomes

$$\begin{aligned} &f_i(\mathbf{x} + \mathbf{e}_i\delta_t, t + \delta_t) - f_i(\mathbf{x}, t) \\ &= (1 - B)\left\{-\frac{1}{\tau}\left[f_i(\mathbf{x}, t) - f_i^{\mathrm{eq}}(\mathbf{x}, t)\right] + \Delta f_i(\mathbf{x}, t)\right\} + B\Omega_i^s \\ &\quad + \delta_t k_i\left(\mathbf{x} + \frac{1}{2}\mathbf{e}_i\delta_t, t + \frac{1}{2}\delta_t\right) + \delta V_i \end{aligned} \tag{22}$$

with

$$\Omega_i^s = f_{\bar{i}}(\mathbf{x}, t) - f_i(\mathbf{x}, t) + f_i^{\mathrm{eq}}(\rho, \mathbf{u}_s) - f_{\bar{i}}^{\mathrm{eq}}(\rho, \mathbf{u}), \tag{23}$$

where $\mathbf{u}_s$ is the velocity of the freezing interface and $\bar{i}$ is the opposite indirection of i. B is a weighting factor related to the volume fraction of solid phase f_s, and f_s is associated with enthalpy, which will be discussed in the next section,

$$B = \frac{\tau - 0.5}{0.5 - f_s + \tau}f_s. \tag{24}$$

The above evolution equation scheme with B is widely applied in the liquid-solid phase change simulations with the LB model [21–28]. In these works, the solid density equals the liquid one. Thus, the total volume of the two phases stays constant because of mass conservation. However, for the water freezing density ratio $\gamma = \rho_s/\rho_l < 1.0$ exists, which results in volume expansion. Here, for our numerical treatment, we first assume the ice density to be the same as the liquid one, and thus the calculated total mass increases as freezing proceeds. By doing so, we can numerically transfer the volume expansion problem to a liquid-solid phase change problem with an additional mass source term accounting for the volume expansion, which is written as δV_i:

$$\delta V_i = f_i^{\mathrm{eq}}(\delta\rho, \tilde{\mathbf{u}}), \tag{25}$$

where $\delta\rho$ denotes the assumed additional mass due to volume expansion and is given by

$$\delta\rho = (1 - \gamma)\rho\frac{\partial f_s}{\partial t}. \tag{26}$$

Because of the additional mass, the simulated freezing solid density appears to be larger than the saturated liquid density ρ_l, resulting in a difference between the obtained expansion volume and the expected value. Therefore, when the density is larger than ρ_l, an approach towards reducing liquid and solid phase compressibility is proposed by calculating the equilibrium distribution function as

$$f_i^{\mathrm{eq}} = \begin{cases} \omega_i\rho_l\left[1 + \frac{\mathbf{e}_i\cdot\mathbf{u}}{c_s^2} + \frac{(\mathbf{e}_i\cdot\mathbf{u})^2}{2c_s^4} - \frac{\mathbf{u}^2}{2c_s^2}\right] & i = 0 \\ \omega_i\frac{\rho - \omega_0\rho_l}{1-\omega_0}\left[1 + \frac{\mathbf{e}_i\cdot\mathbf{u}}{c_s^2} + \frac{(\mathbf{e}_i\cdot\mathbf{u})^2}{2c_s^4} - \frac{\mathbf{u}^2}{2c_s^2}\right] & i \neq 0 \end{cases}. \tag{27}$$

With this treatment of f_i^{eq}, we can readily find that the mass is conserved, while the distribution in surrounding directions is adjusted. When the density is smaller than ρ_l, Eq. (2) is still used.

With the assumption of the volume expansion, the solid phase density needs a correction to obtain the real value and eliminate the effect due to the additional mass source, and the following correction is used:

$$\tilde{\rho} = \rho(1 - f_s + \gamma f_s). \tag{28}$$

D. Enthalpy thermal lattice Boltzmann model

Neglecting the viscous dissipation, we can write the energy equation as [35]

$$\frac{\partial T}{\partial t} + \nabla \cdot (\tilde{\mathbf{u}} T) = \nabla \cdot \left(\frac{\lambda}{\tilde{\rho} c_p} \nabla T \right) + \phi. \tag{29}$$

where λ and c_p are the thermal conductivity and the specific heat capacity, respectively, and ϕ is the source term, which, consists of three parts in the cylindrical coordinate system: The first part is due to the thermal property difference between the gas, liquid, and freezing solid phase. This part ensures continuous heat flux across the interface [18]:

$$\phi_1 = \frac{1}{\tilde{\rho} c_p} \nabla \cdot (\lambda \nabla T) - \nabla \cdot \left(\frac{\lambda}{\tilde{\rho} c_p} \nabla T \right). \tag{30}$$

Based on Eqs. (17) and (18), we can show that this term in the axisymmetric system can be written as

$$\phi_1 = \frac{1}{\tilde{\rho} c_p} \nabla_c \cdot (\lambda \nabla_c T) - \nabla_c \cdot \left(\frac{\lambda}{\tilde{\rho} c_p} \nabla_c T \right) + \frac{1}{r \tilde{\rho} c_p} \frac{\partial (\lambda \nabla_c T)}{\partial r} - \frac{1}{r} \frac{\partial \left(\frac{\lambda}{\tilde{\rho} c_p} \nabla_c T \right)}{\partial r}. \tag{31}$$

The second part of ϕ is due to the liquid-solid phase change associated latent heat:

$$\phi_2 = \frac{\Delta H_{ls}}{c_p} \frac{\partial f_s}{\partial t}. \tag{32}$$

The third part is resulted from the coordinate system transformation given as [36]

$$\phi_3 = -T \frac{\tilde{u}_r}{r} + \frac{\lambda}{r \tilde{\rho} c_p} \nabla T. \tag{33}$$

To solve the energy equation, another distribution function for temperature g_i is used to simulate the thermal field with the evolution equation given by

$$g_i(\mathbf{x} + \mathbf{e}_i \delta_t, t + \delta_t) - g_i(\mathbf{x}, t) = -\frac{1}{\tau_T} \left[g_i(\mathbf{x}, t) - g_i^{\mathrm{eq}}(\mathbf{x}, t) \right] + \delta_t \omega_i \phi. \tag{34}$$

In Eq. (34), g_i^{eq} is the temperature equilibrium distribution function given by

$$g_i^{\mathrm{eq}} = \omega_i T \left[1 + \frac{\mathbf{e}_i \cdot \tilde{\mathbf{u}}}{c_s^2} + \frac{(\mathbf{e}_i \cdot \tilde{\mathbf{u}})^2}{2 c_s^4} - \frac{\tilde{\mathbf{u}}^2}{2 c_s^2} \right], \tag{35}$$

and τ_T is the relaxation time for temperature

$$\tau_T = \frac{3\lambda}{\tilde{\rho} c_p} + 0.5. \tag{36}$$

With the evolution equation (34), the temperature can be calculated by using

$$T = \sum_i g_i. \tag{37}$$

Then the enthalpy can be obtained from the calculated temperature [27]

$$H = f_s c_{p,s} T + (1 - f_s) c_{p,f} T + f_s \Delta H_{ls}. \tag{38}$$

Since the fluid phase contains both liquid and gas phases, to refine the liquid-gas and solid-gas interfaces, the gas fraction f_g is also used to revise the enthalpy as

$$\tilde{H} = f_g (H_l + \Delta H_{gl}) + (1 - f_g) H \tag{39}$$

with

$$f_g = \frac{\rho_l - \rho}{\rho_l - \rho_g}. \tag{40}$$

Using the revised enthalpy, we can express the solid fraction f_s as [27]

$$f_s = \begin{cases} 0 & H \geqslant H_l \\ \frac{H - H_s}{H_l - H_s} & H_s < H < H_l \\ 1 & H \leqslant H_s \end{cases}, \tag{41}$$

where H_l is the liquid phase enthalpy when the solidification phase change starts, and H_s is the solid phase enthalpy when the phase change process ends. The difference between H_l and H_s is the solid-liquid phase change-related latent heat ΔH_{ls}, and the corresponding temperature point (the freezing point) is marked with T_f.

Here we provide a summary of our proposed axisymmetric LB model for simulating the freezing process of a sessile water droplet as detailed in Secs. II A–II C. We first use the classical S-C multiphase model to obtain a liquid-gas two phase system with nonfixed diffuse interface described by Eq. (1). Then through the coordinate transformation from the 2D Cartesian coordinate to the axisymmetric cylindrical coordinate, we extend the S-C multiphase model for simulating the dynamic freezing process of a sessile water droplet with consideration of the volume expansion effect so that the evolution equation (1) is developed into Eq. (22). With Eq. (22) and its relevant equations, the dynamic freezing front and the trijunction point can be obtained. Then the freezing front shape and motion are described by the temperature evolution in the system governed by Eq. (34). The temperature field is used to calculate the solid fraction field (f_s), which connects the mass evolution Eq. (22) and the heat transfer Eq. (34).

III. EXPERIMENTAL SETUP

To validate our proposed LB based numerical model, we conducted experiments for single water sessile droplet freezing on a cold substrate surface (made from silicon wafer) by using a setup schematically illustrated in Fig. 1. The detailed description of the setup can be found in our previous work [37]. In brief, the setup consists of five parts: an enclosed chamber, droplet generation unit, imaging system, gas supply

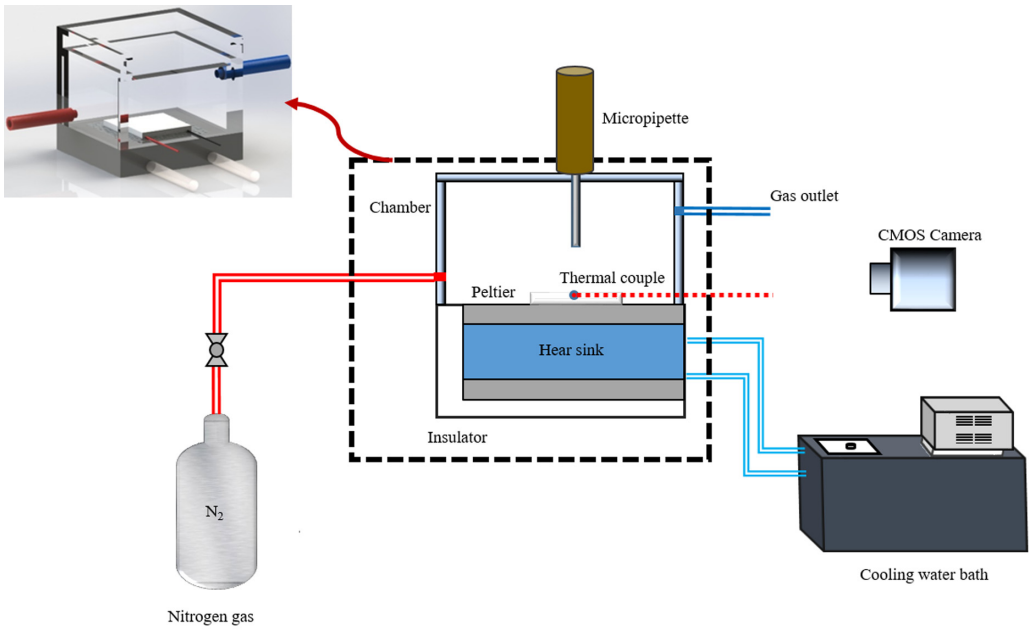

FIG. 1. Schematic of the experimental setup for single water sessile droplet freezing on a subcooled substrate surface.

unit, and thermal control system. The chamber is made from insulating acrylic sheets. Teflon is used as the insulating material to isolate the heat sink. Nitrogen gas is used before the start of experiment to purge vapor in the chamber. With a micropipette, a single droplet a volume of about 4.5 μl is put on the silicon plate whose temperature is maintained at $-15\,^{\circ}$C through a dual cooling achieved by a Peltier and a water bath. The droplet freezing process is recorded by using a high-resolution CMOS camera at a frame rate of 25 fps.

IV. RESULTS AND DISCUSSION

A. Simulation domain, selection of parameters, and description of boundary conditions

In this section, we will use the proposed LBM to simulate the droplet freezing on a cold flat plate as shown in Fig. 2. The size of the simulation domain is described by a lattice number of L_r in the r direction and L_z in the z direction. Before the freezing process begins, the simulation system contains a liquid droplet and a gas phase filled in the rest of the domain space. For the two-phase system, the Peng-Robinson equation of state is used,

$$p = \frac{\rho R_g T_0}{1-b\rho} - \frac{a\rho^2 \varepsilon(T_0)}{1+2b\rho-b^2\rho^2}, \tag{42}$$

where $\varepsilon(T_0) = \{1+(0.37464+1.54226\omega-0.26992\omega^2)[1-(T_0/T_c)^{0.5}]\}^2$, with ω being the acentric factor chosen as 0.344 for water, and R_g is gas constant. Following our previous work [18,38], we choose $a = 2/49$, $b = 2/21$, and $R_g = 1$, and then the fluid-gas density ratio is determined by temperature T_0. Also, the fluid density variation with temperature is assumed to be negligible during the freezing process, and hence the initial temperature T_0 is not involved in the temperature field evolution described in Sec. II C. Here we set $T_0 = 0.85T_c$, which gives the density ratio of $\rho_l/\rho_g = 20$. Because of the low thermal conductivity of the gas phase and negligible liquid-vapor phase change, the higher density ratio has little effect on simulations. On the other hand, a higher saturated temperature can reduce the negative effects of spurious currents in both phases [34].

Initially, the droplet on the surface is of a circular shape with its radius of R_0. The density field is initialized with saturated liquid density ρ_l, the gas phase around it is initialized with saturated vapor density ρ_g, and the droplet interface

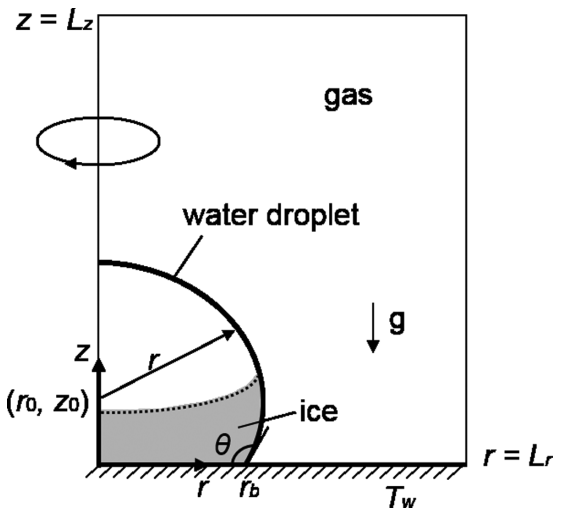

FIG. 2. Schematic of the axisymmetric simulation domain with a water droplet placed on the substrate surface. The boundary conditions used for computations are indicated.

density is expressed as [39]

$$\rho = \frac{1}{2}(\rho_l + \rho_g) - \frac{1}{2}(\rho_l - \rho_g) \times \tanh\left[\frac{2\sqrt{(r-r_0)^2 + (z-z_0)^2} - R_0}{W}\right], \quad (43)$$

where (r_0, z_0) denotes the droplet center coordinates, R_0 is the initial droplet radius, and W is the thickness of interface, which is about 5 in lattice units and thus much smaller than R_0.

As indicated in Fig. 1, the bottom surface denoted by $z = 0$ has constant subcooled temperature T_w and contact angle θ. Here we follow Ding and Spelt [40] to treat such a surface as a diffuse interface, and specifically we obtain the effective mass of every wall lattice (at $z = 0$, and the cells are also regarded as ghost cells adjacent to the solid wall) from the information of its surrounding lattices. The detailed mathematical formulation is given by [40]

$$\psi_{i,0} = \psi_{i,2} + \tan\left(\frac{\pi}{2} - \theta\right)|\psi_{i+1,1} - \psi_{i-1,1}|, \quad (44)$$

where the first and second subscripts, respectively, denote the coordinates tangential and normal to the wall, 0 is the layer on the surface and 1, 2 are the two layers above the surface.

Since the left side of the domain is the axisymmetric axis, the mirror reflection bounce-back boundary condition is used. Furthermore, as $1/r$ is present in several terms in the model formulations (see Sec. II B), the symmetric axis is chosen at a midlattice point $r_0 = 0.5$ instead of $r = 0$. Therefore, the terms associated with $1/r$ should be changed into $1/(r - r_0)$.

For the right and upper sides of the domain, the Neumann boundary is applied as shown in Fig. 2. In the LB scheme, a mixed boundary condition is used by combining the bounce-back boundary with the infinity boundary to ensure better numerical stability, and such a condition is expressed as

$$f_i(\mathbf{x}, t) = \tfrac{1}{2} f_{\bar{i}}(\mathbf{x}, t) + \tfrac{1}{2} f_i(\mathbf{x} - \mathbf{e}_i \delta_t, t). \quad (45)$$

This scheme is also adopted for the temperature boundary of these two sides as

$$g_i(\mathbf{x}, t) = \tfrac{1}{2} g_{\bar{i}}(\mathbf{x}, t) + \tfrac{1}{2} g_i(\mathbf{x} - \mathbf{e}_i \delta_t, t). \quad (46)$$

To convert the lattice units to physical units, the dimensionless length is chosen as the initial droplet radius R_0, the dimensionless time is denoted by the Fourier number, and the dimensionless temperature is defined from the reference temperature T_0 and the surface temperature T_w

$$L^* = \frac{L}{R_0}, \quad t^* = \frac{\lambda_l t}{\rho_l c_p R_0^2}, \quad T^* = \frac{T - T_w}{T_0 - T_w}, \quad (47)$$

where σ is the temperature-dependent surface tension, which is in respect to the reference temperature T_0, and its value $\sigma = 0.0176$ is taken from our previous work [41]. Based on the length scale and temperature, several dimensionless numbers are defined to characterize the freezing process; they include the Bond number, Prandtl number, Fourier number, and Stefan number, respectively, given by

$$\mathrm{Bo} = \frac{gR_0^2(\rho_l - \rho_g)}{\sigma}, \quad \mathrm{Pr} = \frac{\mu_l c_p}{\lambda_l}, \quad \mathrm{Fo} = t^* = \frac{\lambda_l t}{\rho_l c_p R_0^2}, \quad \mathrm{St} = \frac{c_p(T_f - T_w)}{H_{ls}}, \quad (48)$$

With these dimensionless numbers, the gravity acceleration, water dynamic viscosity, thermal conductivity, time, and freezing latent heat can be determined in the simulations. Then the properties of gas and ice phases can be obtained based on their actual ratio with water phase at reference temperature, and a linear interpolation method is applied at the interface as in Ref. [35].

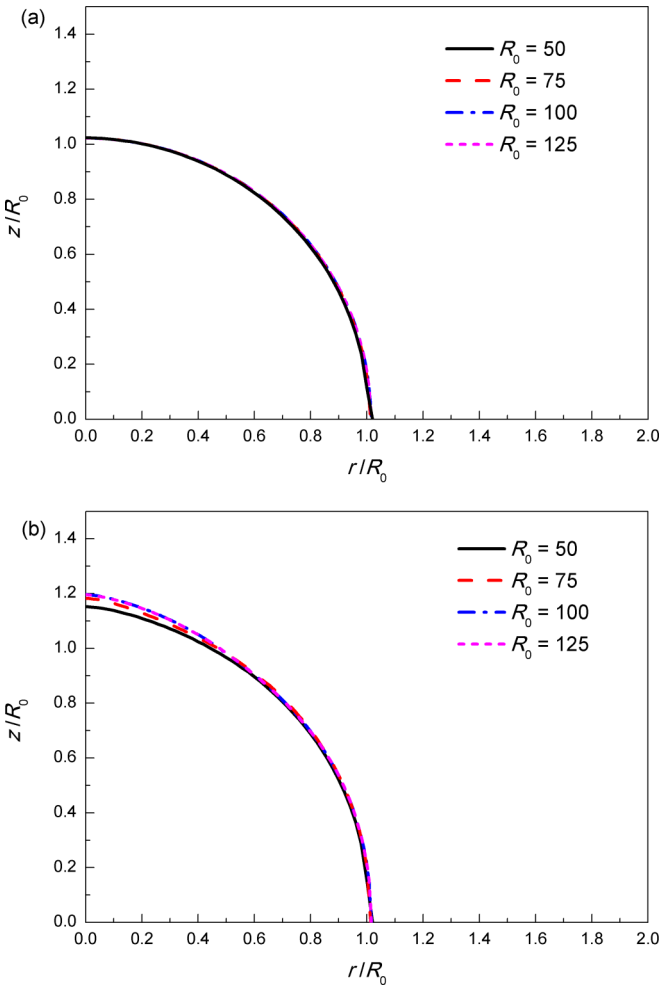

FIG. 3. Water droplet profiles with different grid schemes: (a) before freezing; (b) after freezing.

B. Model validation

To simulate the droplet freezing process with our proposed model, first, the grid independence test is conducted. Figure 3 shows the droplet profiles for four different droplet sizes $R_0 = 50$, 75, 100, and 125 before and after the freezing process. The computation domain has the same ratio as the characteristic length, $L_r = L_z = 2R_0$. Also, the Bond number, Prandtl number, and Stefan number are, respectively, chosen

as Bo = 0.22, Pr = 13.47, and St = 0.19, which are the exact values of those for water at 0 °C. The density ratio of liquid and ice is set as $\gamma = 0.9$, and the contact angle is $\theta = 90^\circ$. At beginning, a hemispherical droplet with its radius of R_0 is placed on the bottom surface as described in Sec. IV A. Then the bottom surface is imposed with a given contact angle θ and temperature T_0, and nearly 30 000 steps are needed to ensure that the droplet reaches its steady state on the surface. In the following, the surface temperature reduces to T_w. When the temperature at the droplet's bottom falls to the freezing point T_f, the enthalpy of this location decreases and also releases latent heat, indicating that the icing process occurs.

As shown in Fig. 3(a), the four droplet profiles, which are drawn using the average density between gas and liquid under a stationary state, namely, $\rho = (\rho_l + \rho_g)/2$, are almost coincident with each other in a dimensionless scale. However, Fig. 3(b) shows a noticeable difference in the frozen droplet profile for different values of R_0. Specifically, for the coarse grids (i.e., $R_0 < 100$), the tip of the droplet is at a lower position compared to the dense grids. This is because the droplet with a smaller R_0 takes much less time for its freezing process, leading to a larger ice density than what is expected, since the increasing mass on the freezing front is unable to enter the liquid phase quickly. Nonetheless, the grid independence is verified when R_0 is larger than 100. Therefore, the characteristic length is chosen as $R_0 = 100$; this gives the computation square as $L_r \times L_z = 200 \times 200$, which will be used in the following simulations.

Figure 4(a) depicts the evolution of droplet freezing process at different stages. Since the simulated total freezing time is $t^* = 76$, we choose three intermediate time points as $t^* = 19$, 38, and 57, corresponding to dash, dot, and dash dot lines, respectively. As time elapses, the liquid-ice freezing front moves upwards, and the ice edge (i.e., the triple contact line point) deviates from its original profile more and more because of the volume expansion effect. The shape of the freezing front interface changes from nearly flat to concave, indicating a larger freezing velocity at the edge than that in the center. Then the freezing front keeps the concave shape and moves upward, which also can be seen in the simulation results by other researchers [12–15]. Shown in Fig. 4(b) is the computed droplet volume change with its definition as $V = \iint 2\pi r dr dz$ for both liquid water and solid ice phases. V_0 is the liquid droplet volume at $t^* = 0$. Clearly, the speed of volume expansion decreases with increasing time. For instance, at the middle point $t^* = 38$, more than two-thirds of the droplet undergoes the phase change. When the freezing process is completed, the volume ratio V/V_0 approaches the density radio of liquid and ice density $1/\gamma$. This also verifies the mass conservation achieved by using our axisymmetric LB model for the freezing process with density change. Figures 4(c) and 4(d), respectively, show the dimensionless temperature (T^*) and enthalpy [$H^* = (H - H_0)/H_{fg}$] contours in the simulation domain at the time point $t^* = 38$. The solid and dashed lines in Fig. 4(c) denote the droplet profile and the freezing front in the droplet, respectively, which are completely coincident with the enthalpy interfaces in Fig. 4(d). Temperature in the droplet is continuous, and its highest value is located near the top part. The temperature gradient below the freezing front is small, indicating the latent

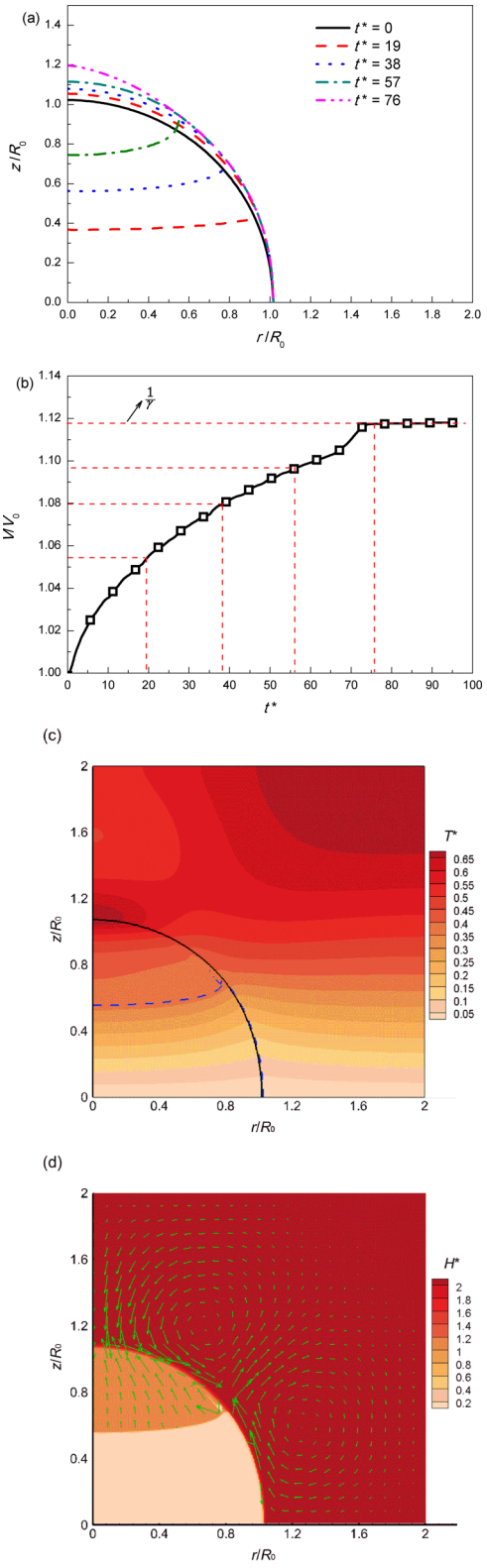

FIG. 4. Simulated droplet freezing process on the substrate surface of contact angle $\theta = 90^\circ$ with the ice-water density ratio $\gamma = 0.9$: (a) time evolution of the droplet profiles at different freezing stages (time, with the simulated total freezing time as $t^* = 76$); (b) droplet volume change during the entire freezing process (here V_0 is the original liquid droplet volume at $t^* = 0$); (c) temperature contours at $t^* = 38$; (d) enthalpy contours and velocity vectors at $t^* = 38$.

heat dissipation from the front to the substrate. However, the enthalpy is nearly uniform in each phase but has obvious differences between ice, water, and gas. We also present the velocity vectors in the simulation domain in Fig. 4(d). To make the velocity field clearer, the velocity value in water and ice is shown with 10×, while the velocity in the gas remains the same. Clearly, there is no interflow in the ice, and the flow in the water moves upward due to the volume expansion at the freezing front.

C. Comparison with experimental results

It is known that the density ratio of pure water and ice is about $\gamma = 0.916$. Considering dissolved gas in water inevitably to expand into visible bubbles in ice, the actual volume ratio before and after freezing may be larger. This can be confirmed by comparing the images of the water and ice droplets after excluding the condensation factor. In our experiments, the real volume ratio is about 0.895 according to the volume comparison between before and after freezing. In addition, before the freezing front appears, a nucleation stage, also called the recalescence stage, occurs. In this stage, liquid water turns into a mixture of water and ice. Since the nucleation time is much shorter compared to the whole freezing period, this makes it difficult to simulate such a small timescale. Hence, the numerical simulation takes the time right before the nucleation stage as the initial state.

With the simulation conditions set with the same dimensionless values, Fig. 5 compares the experimental images (here the dashed lines indicate the horizontal freezing front) with the numerical simulation results and is shown in Fig. 5. In particular, Figs. 5(a) and 5(b) present the freezing evolution on a hydrophilic surface ($\theta = 64^\circ$) and a hydrophobic surface ($\theta = 98^\circ$), respectively, in each figure the left side being the experimental images and the right side being the simulation results. A quantitative comparison of the experimental and simulation results for the final droplet height shows the largest relative errors, respectively, as 1.6% and 2.0% for the hydrophilic and hydrophobic cases, indicating a reasonable agreement between the experiments and the simulations. Moreover, with introducing τ^* as the dimensionless time with respect to the total freezing time, we obtain the total freezing time in our experiment and simulation as $t^* = 60.1$ and $t^* = 51.4$ on the hydrophilic surface, respectively; $t^* = 85.2$ and $t^* = 87.3$ on the hydrophobic surface, respectively. Also, gas bubbles are seen in the experimental figures. The freezing front inside the droplet is of concave shape. The formation of the pointed cone after the freezing ($\tau^* = 1.0$) is very similar in both hydrophilic and hydrophobic cases. Considering that our model is based on axisymmetric coordinates, the droplet shape change is in line with the actual volume expansion coefficient, i.e., the density ratio of liquid and ice $1/\gamma$.

Figure 6 gives comparisons between experiments and simulations for the freezing front dimensionless height and radii during freezing process. On the hydrophilic surface shown in Fig. 6(a), the numerical and experimental curves are nearly coincident with each other except for the final stage. The freezing front radii exhibit almost linear time dependence, and the freezing front height increases with time at a gradually reducing speed. On the hydrophobic surface shown in Fig. 6(b),

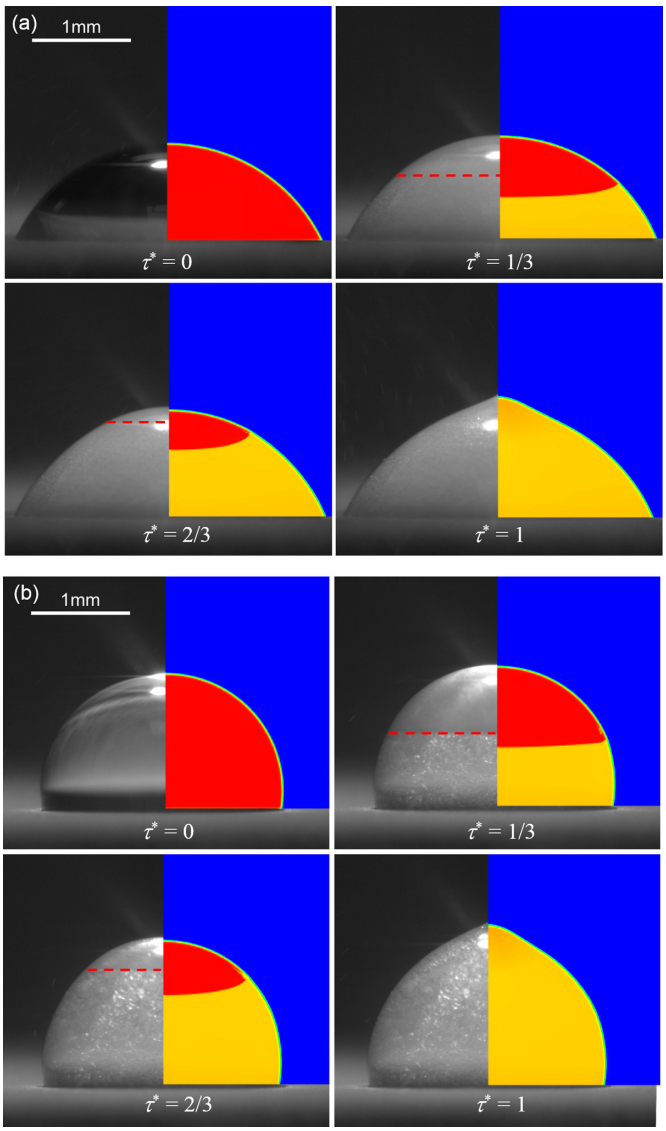

FIG. 5. Comparison of water droplet freezing shapes at different times between experiment (left) and simulation (right): (a) substrate contact angle $\theta = 64^\circ$; (b) substrate contact angle $\theta = 98^\circ$.

though both the numerical and experimental curves show the same trends as those in Fig. 6(a), the difference between the numerical and the experimental results is larger, with the largest relative error of about 13% in the dimensionless freezing front height. In both Figs. 6(a) and 6(b), at the early stage, the experimental and numerical freezing front positions are almost overlapping each other, and then the difference between them gradually gets larger. The reason lies in that the freezing process starts experimentally from the nucleation stage, and within this stage the droplet with certain expansion occurs in a very short time. An ice skeleton is present inside the unfreezing water phase, thereby enhancing heat transfer and reducing the water-ice latent heat released. These effects lead to a smaller St number in the experiment than in the simulation, resulting in a lower freezing velocity in the simulation during most portion of the freezing period. However, the simulated freezing velocity in the final stage significantly increases on both surfaces, indicating that the freezing front

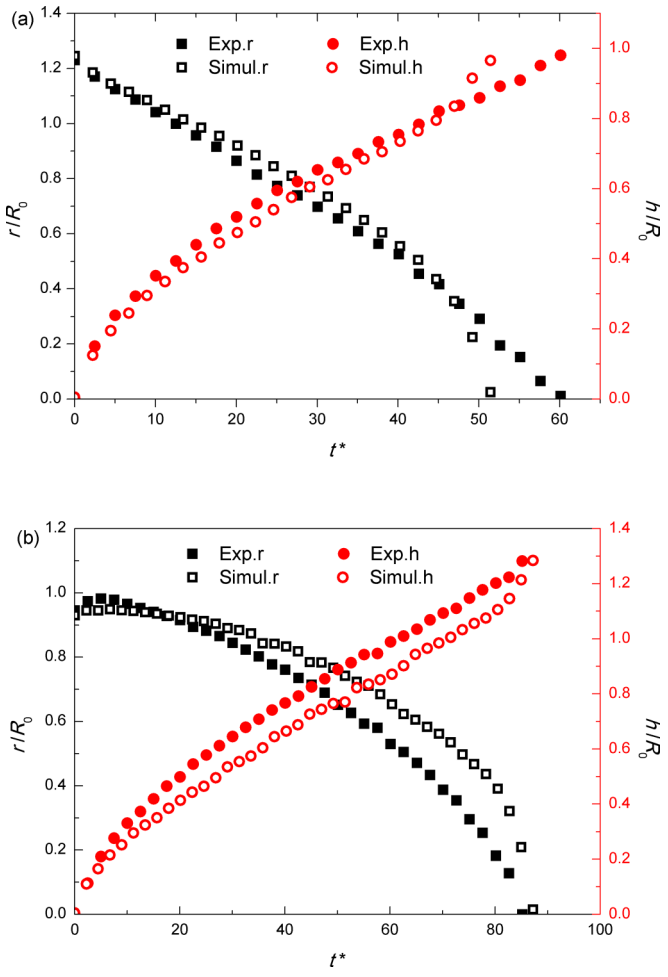

FIG. 6. Comparison of the droplet freezing front height and radii between experimental and simulation results: (a) substrate contact angle $\theta = 64^\circ$; (b) substrate contact angle $\theta = 98^\circ$.

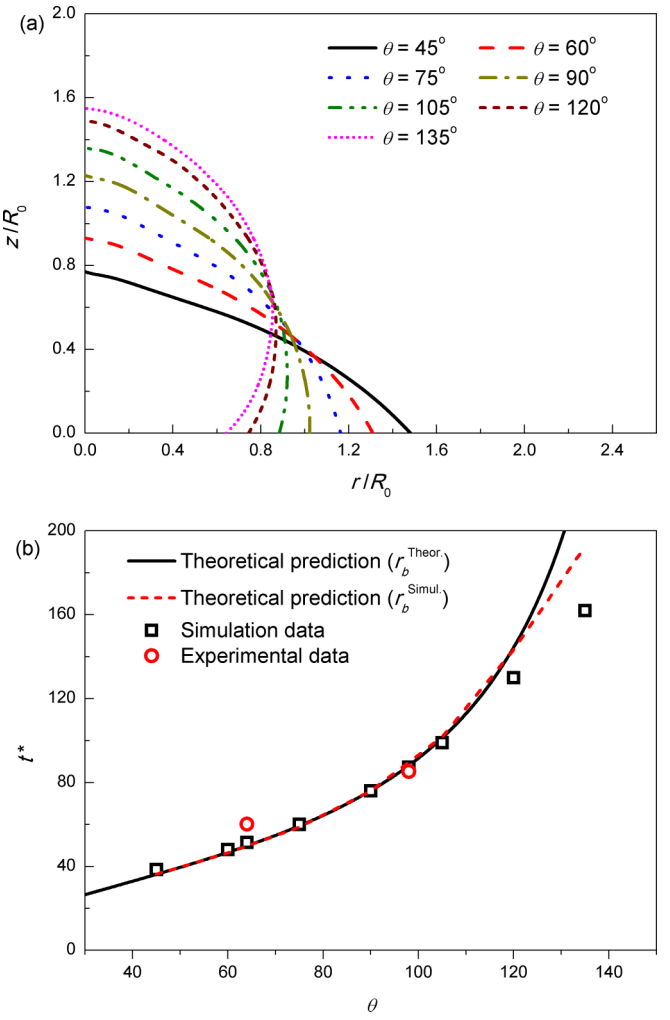

FIG. 7. Droplets with the same initial volume on the substrate surface of different contact angle: (a) final frozen droplet shapes; (b) total freezing time versus contact angle with a comparison among the simulations, theoretical predictions, and experiments.

approaches the droplet's top rapidly. This transition is due to the enthalpy model used to deal with the liquid-solid phase change. In the final stage, the unfrozen water remains negligibly on the droplet's top, and its temperature reduces to the freezing temperature. Liquid enthalpy decreases at a larger velocity, and the fraction fs increases to unit one rapidly. Evidently, in Zhang *et al.*'s simulation with the VOF model, similar results on the front moving were also observed in the final freezing stage [15].

D. Effects of surface wettability and volume expansion on droplet freezing

To examine the effect of surface wettability, we conducted the simulations with different contact angles varying from $\theta = 45^\circ$ to $\theta = 135^\circ$, while keeping the droplet volume and dimensionless numbers unchanged. For the superhydrophilic or superhydrophobic surfaces with smaller or larger contact angle, the droplet interface becomes very close to the domain boundary, leading to large computation errors because of the need of calculating tangential values with Ding and Spelt's scheme [40]. Figure 7(a) depicts the frozen droplet profiles with the same droplet volume and the density ratio $\gamma = 0.9$ for different contact angles. With increasing the contact angle, the bottom radius r_b and the height h_t of the frozen droplet decreases and increases, respectively. The total freezing time for a droplet on the surface with various contact angles is presented in Fig. 7(b), which shows the freezing time increases rapidly with increasing the contact angle. Under the assumption of pseudo-steady, 1D conduction heat transfer in the ice, the problem is simplified to a one-zone solidification problem, and thus we can obtain the linear temperature distribution in ice and thus constant cooling flux from the subcooled surface to the droplet. Then the freezing time can be estimated by using the thermal energy balance

$$t = \frac{\rho V H_{fg}}{\pi r_b^2 q''} \tag{49}$$

in which the numerator part is the total latent heat released during freezing and the denominator part is the heat transferred to the cold substrate surface per unit time. Neglecting the gravity effect, we can treat the droplet as a spherical cap and hence obtain a relationship between its volume V and

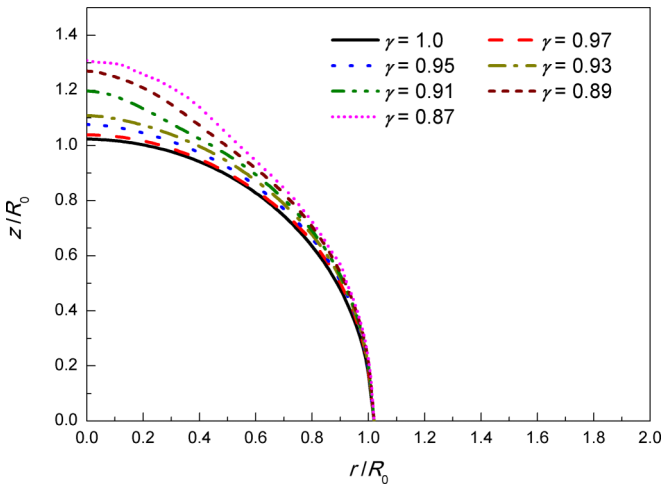

FIG. 8. Droplet frozen shapes for different volume expansion coefficient on the substrate surface of contact angle $\theta = 90^\circ$.

bottom radius r_b as

$$V = r_b^3 f_V(\theta) = \frac{\pi r_b^3}{3}\left(\frac{2 - 3\cos\theta + \cos^3\theta}{\sin^3\theta}\right). \quad (50)$$

Combining Eqs. (49) and (50), we can analytically estimate the dimensionless total freezing time $t*$ (with respect to $\theta = 90^\circ$) as a function of contact angle, which is displayed as the solid line in Fig. 7(b). Moreover, based on the numerically simulated r_b and Eq. (49), another prediction of $t*$ is plotted in the dash line for a comparison. The comparison results show that except for lager contact angle cases (i.e., $\theta > 130^\circ$), both the numerically simulated results and the analytical predictions can well capture the trend of our experimental results (note: the largest relative error is within 20%). The differences result from the facts that for high contact angles, the droplet height h_t becomes larger and the droplet contact area with the bottom surface get much smaller. More specifically, on the one hand, a larger h_t is associated with a longer diffusion heat time $t_{\text{diff}} \sim {h_t}^2$ and also the possible presence of temperature gradient in the liquid zone. On the other hand, a smaller contact surface area likely causes more complicated heat transfer, both leading to violation of the assumption of pseudo-steady, 1D conduction heat transfer in the ice, which in turn gives rise to a smaller freezing time than the predicted value.

As for the effect of volume expansion coefficient γ, Fig. 8 shows such an effect on the final frozen droplet profiles with different γ values ($0.87 \leqslant \gamma \leqslant 1.0$) for the droplets with the same radius $R_0 = 100$ and contact angle $\theta = 90^\circ$. When there is no volume expansion ($\gamma = 1.0$), the frozen droplet keeps the same shape as the water droplet. As γ reduces, the frozen droplet shape changes with rising the droplet height. The droplet's top shape remains smooth when $\gamma > 0.91$. When $\gamma \leqslant 0.91$, the cone-shape tip appears on the frozen droplet. This suggests that the surface tension indeed has a suppression effect on the formation of droplet cone shape, and it plays a dominant role when γ is not large enough ($\gamma \leqslant 0.91$).

Additionally, we study the cone angle of frozen droplet tip. Marin *et al.* [10] provided a theoretical analysis of the tip formation based on a geometric illustration shown in Fig. 9(a).

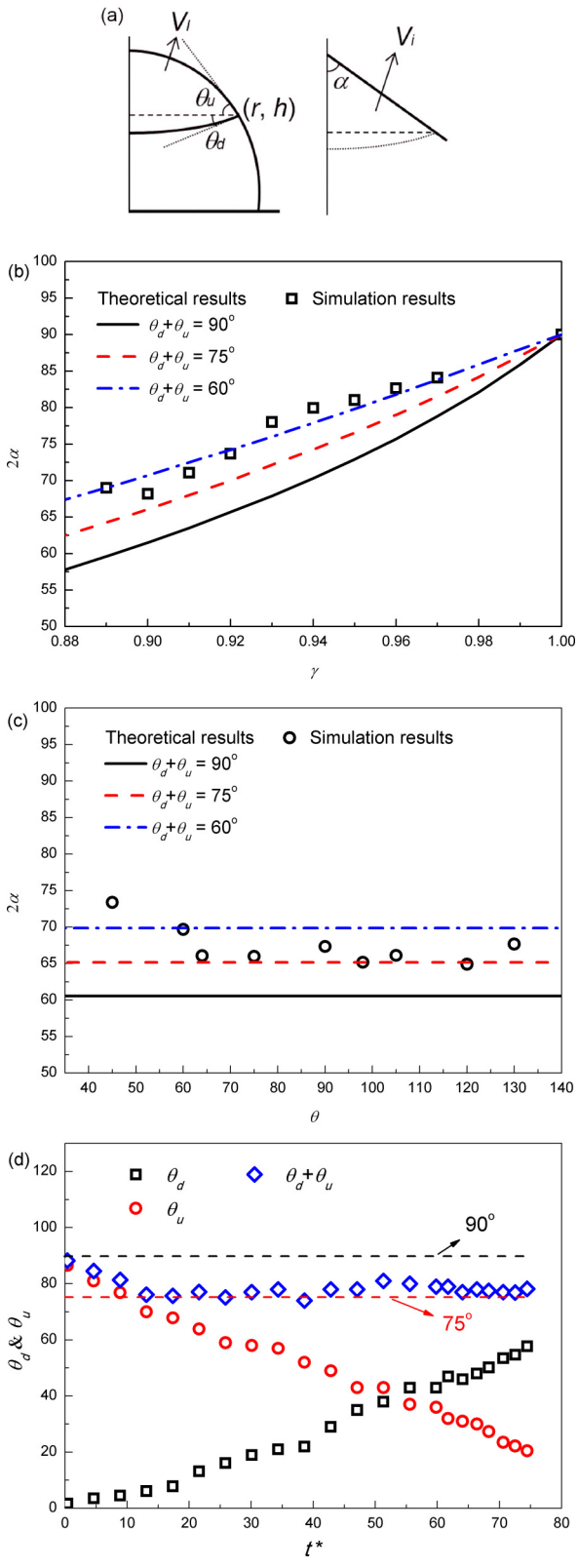

FIG. 9. Cone angle 2α formed on the frozen droplet: (a) sketch of the tip geometry on the droplet at the last freezing stage with the freezing front-to-interface angle indicated as $\theta_u + \theta_d$ [10]; (b) cone angle versus volume expansion coefficient; (c) cone angle versus contact angle; (d) time evolution of angles θ_u and θ_d for the case $\theta = 90^\circ$ and $\gamma = 0.9$.

When close to the final stage of freezing, the remained liquid volume V_l is assumed to have two parts: a spherical cap and a circular truncated cone with two angles θ_u and θ_d, and hence V_l can be expressed as

$$V_l = r^3 f_V(\theta_u) + r^3 f_V(\theta_d), \tag{51}$$

where the function f_V is given in Eq. (50). After the freezing completes, the solid ice volume V_i is assumed to be the sum of a spherical cone and the same circular truncated cone as in V_l, and hence V_i can be given by

$$V_i = \frac{\pi}{3}\frac{r^3}{\tan\alpha} + r^3 f_V(\theta_d), \tag{52}$$

where α is half of the cone angle. The two volumes have the relationship of $V_l = \gamma V_i$, based on which together with Eqs. (51) and (52) we can get α. Figures 9(b) and 9(c) present the simulated cone angle 2α versus density ratio γ (while keeping a fixed $\theta = 90^\circ$) and contact angle θ (while keeping a fixed $\gamma = 0.9$), respectively. Also, in Figs. 9(b) and 9(c), the lines denote the theoretical predictions calculated from the analytical model given in Eq. (51) and Eq. (52). It should be noted that in Marin *et al.*'s analysis [10], the freezing front-to-interface angle, i.e., $\theta_u + \theta_d$, is assumed to be 90°, which is in line with their 2D-like Hele-Shaw cell experimental observations. Our simulations for an axisymmetric droplet (i.e., 3D simulations), however, show much differently from the predicted line $\theta_u + \theta_d = 90^\circ$. Instead, the simulated cone angle 2α is closer to the lines of $\theta_u + \theta_d = 60^\circ$ and $\theta_u + \theta_d = 75^\circ$ [Fig. 9(b)]. Moreover, as shown in Fig. 9(c), a nearly constant cone angle of about 65° is obtained within a range of $\theta = 60^\circ$ to $\theta = 130^\circ$, which agrees well with the predicted dash line of $\theta_u + \theta_d = 75^\circ$. To further explore the reason causing such difference, we present the time evolution of freezing front angles, θ_u and θ_d, during the whole freezing process for the case of $\theta = 90^\circ$ and $\gamma = 0.9$ in Fig. 9(d). As the freezing front moves up, θ_u decreases from about 90° to 20°, and at the same time θ_d increases from zero to about 60°. During the most freezing period, the sum $\theta_u + \theta_d$ keeps about 75°. This matches well with those results presented in Figs. 9(b) and 9(c). Therefore, our simulation results suggest that the freezing front-to-interface angle $\theta_u + \theta_d$ does not simply keep at 90° even at the final stage of freezing. This conclusion was experimentally supported by Zhang *et al.*'s [42] recent work.

In Marin *et al.*'s [6] self-similar freezing dynamic analysis on a droplet, the frozen part is assumed to be of a conical shape, and the freezing front forms a spherical surface centered at the cone tip. Thus, the two surfaces (the cone surface and the freezing front) are perpendicular to each other, making $\theta_u + \theta_d = 90^\circ$ naturally. Based on the assumptions, each part of $\theta_u + \theta_d$ should also be constant as θ_u is equal to $90^\circ - \alpha$. However, an accurate measurement of θ_d is difficult in a free sessile freezing droplet, and the confined freezing experiment in a 2D Hele-Shaw cell inevitably affects the two angles at a triple contact line. Based on our simulations, though their sum remains a nearly constant value, both θ_u and θ_d individually change even in the final stage. As the trijunction shrinks continuously to finally become a single point, the assumed cone tip's location keeps rising because of the volume expansion. At the same time, the angle θ_u will also be changed accordingly. Moreover, the variation of θ_d indicates the normal velocity of the freezing front is not uniform at different radius locations. Then the freezing front shape cannot be treated as spherical at a different time. Further research is needed on this issue.

V. CONCLUDING REMARKS

In this work, we have proposed an axisymmetric lattice Boltzmann model for describing liquid-solid phase change problems to simulate the freezing process of a sessile droplet with volume expansion. We have validated the proposed model by carrying out both grid independence and mass conservation tests. Also, we have made a comparison between the LB simulations and the experiments of the frozen droplet shape and freezing front results for a sessile water droplet freezing on both hydrophilic and hydrophobic subcooled surfaces and obtained reasonable agreement. In addition, we have used both our proposed LB model and our derived analytical models to examine the effects of contact angle and volume expansion coefficient on the droplet freezing time and the cone angle of frozen droplet tip. The analytical models for the droplet freezing time and the cone angle of a frozen droplet tip are derived based on thermal energy balance and geometric analysis, respectively. The results show that except for large contact angle cases (i.e., $\theta > 130^\circ$), both the simulated results and the analytical predictions can well capture our experimental trend for the freezing time, which rises rapidly with increasing contact angle. However, above $\theta > 130^\circ$, the assumptions used for deriving the analytical model of the droplet freezing time become invalid. Finally, we have shown that the droplet volume expansion has noticeable effect on the cone angle. Both our LB simulations and analytical model predictions have shown that during the droplet freezing, the freezing front-to-interface angle, $\theta_u + \theta_d$, does not stay at 90°, which was assumed by Marin *et al.* [10].

ACKNOWLEDGMENT

This work was supported by the Ministry of Singapore via Tier 2 Academic Research Fund (MOE2016-T2-1-114).

[1] Y. Lin, H. Chen, G. Wang, and A. Liu, Coatings **8**, 208 (2018).
[2] P. Hao, C. Lv, and X. Zhang, Appl. Phys. Lett. **104**, 161609 (2014).
[3] Y. Wang and Z.-G. Wang, J. Coat. Technol. Res. **16**, 869 (2019).
[4] L. Huang, Z. Liu, Y. Liu, Y. Gou, and L. Wang, Exp. Therm. Fluid Sci. **40**, 74 (2012).
[5] S. Wildeman, S. Sterl, C. Sun, and D. Lohse, Phys. Rev. Lett. **118**, 084101 (2017).

[6] D. Anderson, M. G. Worster, and S. Davis, J. Cryst. Growth **163**, 329 (1996).
[7] M. Nauenberg, Eur. J. Phys. **37**, 045102 (2016).
[8] A. Schetnikov, V. Matiunin, and V. Chernov, Am. J. Phys. **83**, 36 (2015).
[9] J. H. Snoeijer and P. Brunet, Am. J. Phys. **80**, 764 (2012).
[10] A. G. Marin, O. R. Enriquez, P. Brunet, P. Colinet, and J. H. Snoeijer, Phys. Rev. Lett. **113**, 054301 (2014).
[11] M. Tembely and A. Dolatabadi, J. Fluid Mech. **859**, 566 (2018).
[12] T. V. Vu, G. Tryggvason, S. Homma, J. C. Wells, and H. Takakura, J. Chem. Eng. Jpn. **46**, 726 (2013).
[13] T. V. Vu, G. Tryggvason, S. Homma, and J. C. Wells, Int. J. Multiphase Flow **76**, 73 (2015).
[14] X. Zhang, X. Wu, J. Min, and X. Liu, Appl. Therm. Eng. **125**, 644 (2017).
[15] X. Zhang, X. Liu, X. Wu, and J. Min, Int. J. Heat Mass Transfer **127**, 975 (2018).
[16] Y. Zhao and C. Yang, arXiv:1712.04268 (2017).
[17] S. K. Singha, P. K. Das, and B. Maiti, Langmuir **34**, 9064 (2018).
[18] C. Zhang and P. Cheng, Int. J. Heat Mass Transfer **110**, 319 (2017).
[19] X. Liu and P. Cheng, Int. J. Heat Mass Transfer **64**, 1041 (2013).
[20] C. Zhang, F. Hong, and P. Cheng, Int. J. Heat Mass Transfer **86**, 629 (2015).
[21] D. Chatterjee and S. Chakraborty, Phys. Lett. A **341**, 320 (2005).
[22] D. Chatterjee and S. Chakraborty, Int. J. Therm. Sci. **47**, 552 (2008).
[23] T. Lei, K. H. Luo, and D. Wu, Phys. Rev. E **99**, 053301 (2019).
[24] X. Zhao, B. Dong, W. Li, and B. Dou, Appl. Therm. Eng. **111**, 1477 (2017).
[25] P. Xu, S. Xu, Y. Gao, and P. Liu, Int. J. Heat Mass Transfer **127**, 136 (2018).
[26] J. Sun, J. Gong, and G. Li, Int. J. Refrig. **59**, 53 (2015).
[27] X. Li, J. Zhao, and P. Cheng, Int. J. Heat Mass Transfer **114**, 628 (2017).
[28] W. Xiong and P. Cheng, Int. J. Heat Mass Transfer **124**, 1262 (2018).
[29] J. Gong, J. Hou, L. Yang, W. Wu, G. Li, and T. Gao, J. Mech. Sci. Technol. **33**, 1925 (2019).
[30] X. Shan and H. Chen, Phys. Rev. E **49**, 2941 (1994).
[31] A. L. Kupershtokh and D. A. Medvedev, J. Electrost. **64**, 581 (2006).
[32] S. Srivastava, P. Perlekar, J. H. M. ten Thije Boonkkamp, N. Verma, and F. Toschi, Phys. Rev. E **88**, 013309 (2013).
[33] S. A. Reijers, H. Gelderblom, and F. Toschi, J. Comput. Sci. **17**, 309 (2016).
[34] S. Gong and P. Cheng, Comput. Fluids **53**, 93 (2012).
[35] S. Gong and P. Cheng, Int. J. Heat Mass Transfer **55**, 4923 (2012).
[36] Q. Li, Y. L. He, G. H. Tang, and W. Q. Tao, Phys. Rev. E **80**, 037702 (2009).
[37] Y. Zhao, R. Wang, and C. Yang, Int. J. Heat Mass Transfer **108**, 1048 (2017).
[38] C. Zhang, P. Cheng, and W. J. Minkowycz, Int. J. Heat Mass Transfer **115**, 500 (2017).
[39] A. Xu, T. S. Zhao, L. An, and L. Shi, Int. J. Heat Fluid Flow **56**, 261 (2015).
[40] H. Ding and P. D. M. Spelt, Phys. Rev. E **75**, 046708 (2007).
[41] C. Zhang, P. Cheng, and J. Cao, Int. Commun. Heat Mass Transfer **78**, 295 (2016).
[42] X. Zhang, X. Liu, J. Min, and X. Wu, Appl. Therm. Eng. **147**, 927 (2019).